



Internal kinematics of *Gaia* eDR3 wide binaries

X. Hernandez,¹★ S. Cookson² and R. A. M. Cortés¹ 

¹*Instituto de Astronomía, Universidad Nacional Autónoma de México, Apartado Postal 70–264 C.P., 04510 México D.F. México*

²*Crawley Astronomical Society, c/o Copthorne Prep Sch, Effingham Ln, Copthorne, Crawley RH10 3HR, UK*

Accepted 2021 October 15. Received 2021 October 12; in original form 2021 July 30

ABSTRACT

Using the recent *Gaia* eDR3 catalogue, we construct a sample of solar neighbourhood isolated wide binaries satisfying a series of strict signal-to-noise data cuts, exclusion of random association criteria, and detailed colour–magnitude diagram selections to minimize the presence of any kinematic contaminating effects having been discussed in the literature to date. Our final high-purity sample consists of 423 binary pairs within 130 pc of the sun and in all cases high-quality *Gaia* single-stellar fits for both components of each binary (final average RUWE values of 0.99), both also restricted to the cleanest region of the main sequence. We find kinematics fully consistent with Newtonian expectations for separations, s , below 0.009 pc, with relative velocities scaling with $\Delta V \propto s^{-1/2}$ and a total binary mass, M_b , velocity scaling consistent with $\Delta V \propto M_b^{1/2}$. For the separation region of $s > 0.009$ pc, we obtain significantly different results, with a separation independent $\Delta V \approx 0.5 \text{ km s}^{-1}$ and a $\Delta V \propto M_b^{0.24 \pm 0.21}$. This situation is reminiscent of the low acceleration galactic baryonic Tully–Fisher phenomenology, and indeed, the change from the two regimes we find closely corresponds to the $a \lesssim a_0$ transition. These results are at odds not only with Newtonian expectations, but also with MOND predictions, where the presence of an external field effect implies only small deviations from Newtonian dynamics are expected for solar neighbourhood wide binaries.

Key words: gravitation – binaries: general – stars: kinematics and dynamics.

1 INTRODUCTION

The most salient features of the gravitational anomalies generally ascribed to the presence of a dominant dark matter component at galactic scales, are the loss of a dependence on radius for equilibrium velocities, the clear scaling of these equilibrium velocities with the fourth root of the total baryonic mass of the systems in question, and the occurrence of the transition from a regime where the observed matter alone adequately explains kinematic observations through Newtonian gravity, to the aforementioned anomalous region, always at acceleration scales of $a = a_0 \approx 1.2 \times 10^{-10} \text{ m s}^{-2}$.

The first two of the above properties are of course the well-known flatness and baryonic Tully–Fisher relation of late-type galactic rotation curves, which can be summarized as $V_{\text{TF}} = 0.35(M/M_\odot)^{1/4} \text{ km s}^{-1}$ (McGaugh et al. 2000), and which have been recently extended to the asymptotically flat velocity dispersion profiles of a variety of pressure supported systems such as globular clusters (e.g. Scarpa et al. 2003, Hernandez et al. 2012b, Hernandez & Lara-Díez et al. 2020) and elliptical galaxies (e.g. Jimenez et al. 2013; Durazo et al. 2018; Chae et al. 2020a), also showing a scaling with the fourth root of the total baryonic mass.

The last of the three traits described above forms the basis of MOND (Milgrom 1983) as an alternative to the standard dark matter postulate, where an underlying transition in the structure of physics is proposed as the causal mechanism behind the gravitational anomalies that occur in the low acceleration regime at galactic scales, and forms also the central tenant of a large range of modified gravity theories

inspired by MOND, aiming at an explanation in the absence of the dark matter hypothesis. Examples of these last are Bekenstein (2004), Moffat & Toth (2008), Zhao & Famaey (2010), Capozziello & De Laurentis (2011), Verlinde (2016), Barrientos & Mendoza (2018), McCulloch et al. (2019), and Hernandez et al. (2019b).

Within the context described above, one of us in Hernandez et al. (2012a) identified wide binaries as an interesting test case to explore the generality (or lack thereof) of the gravitational anomalies detected at galactic scales, to an entirely different astronomical range of scales and masses, which, however, shares the same low acceleration regime. Wide binaries composed of two $1 M_\odot$ mass stars will cross the $a < a_0$ threshold when the separation between both components, s , becomes larger than about 7000 au, 0.035 pc, Hernandez et al. (2012a). That initial exploration of the problem was performed using the best astrometry available at the time, that from the *Hipparcos* satellite. The results were for 1D relative velocities on the plane of the sky for a small carefully selected sample of 280 wide binaries, showing values much larger than Newtonian expectations, and, to within the large confidence intervals of that study, consistent with no dependence on the separation on the plane of the sky of the two components of the binaries studied, for separations well within the tidal radius of the problem, of about 0.7 pc (e.g. Jiang & Tremaine 2010).

Since, the interest on the proposed test has grown and a number of independent investigations have been performed, confirming the presence of the signal first detected in Hernandez et al. (2012a). Scarpa et al. (2017) performed detailed ground based follow-up observations of a small sub-sample of the stars analysed in Hernandez et al. (2012a), obtaining accurate spectroscopic line of sight velocities, and confirming the presence of relative 3D velocities in excess of Newtonian expectations. Pittordis & Sutherland (2018),

★ E-mail: xavier@astro.unam.mx

Banik & Zhao (2018), and Banik & Kroupa (2019) refined the original test and conclude that distinguishing between Newtonian and modified gravity models will be possible using final *Gaia* data, once the full mission accuracy becomes available. Using *Gaia* DR2 data, Pittordis & Sutherland (2019) show that some MOND variants appear disfavoured by their analysis of wide binaries, while the uncertainties inherent to the data used were unable to unequivocally discern between a purely Newtonian scenario and some MOND variants. More recently, in Hernandez et al. (2019a) two of us revisited the wide binary sample of the original experiment, but using the much superior *Gaia* DR2 astrometry, and obtaining results consistent with the original, in spite of substantially reduced confidence intervals on the relative velocities.

For relatively bright unresolved stellar companions, the position of the observed star in the HR diagram will shift to brighter magnitudes as per standard spectroscopic binaries, while for sufficiently dim undetected companions (essentially stellar dark matter), the wobble induced on the affected component of the observed binary, a kinematic contamination inflating the detected binary kinematics, will become apparent through the quality of the fit of the single star solution. In more detail, Belokurov et al. (2020) show that unresolved stellar companions in the *Gaia* DR2 catalogue result in poor single stellar fits (RUWE values larger than 1.4, extending to 10 or sometimes even larger, the renormalized unit weight error parameter of *Gaia*), and identify regions of the solar neighbourhood *Gaia* HR diagram where unresolved stellar companions are prominent, and regions where such companions are largely absent.

In this paper, we use the recent *Gaia* eDR3 (*Gaia* Collaboration 2016, 2020, 2021; Lindegren et al. 2021) catalogue to construct a large sample of 5844 nearby, locally isolated wide binaries having high quality radial velocities, parallaxes, colours, magnitudes and proper motions, to construct a detailed picture of their relative velocity on the plane of the sky, ΔV . This, as a function of both 2D projected separation and total binary mass, M_b , the latter as a diagnostic tool to help derive physical insight into the trends observed in velocity as a function of binary separation, with stellar mass inferred from main sequence accurate estimates through the absolute G magnitude from Pittordis & Sutherland (2019).

The initial sample is then carefully pruned to minimize all sources of kinematic contamination discussed to date, a strict RUWE parameter upper limit designed to exclude short period blended tertiaries, relative radial velocity cuts to exclude contamination of unbound stars from the mean field local distribution, and a detailed HR diagram region selection to further exclude the presence of unresolved stellar companions, restricted to the cleanest section of the main sequence, always for both components of each nearby binary. Results are consistent with Newtonian expectations in both separation and mass relative velocity scalings for the low separations corresponding to a high acceleration regime, but reminiscent of Tully–Fisher scalings for the low acceleration regime of wide binary separations.

In Section 2, we present our initial sample selection describing the removal of binaries in clustered environments to produce a catalogue of relatively isolated binaries, the use of a relative velocity along the line-of-sight threshold to exclude chance associations of unbound systems, and the introduction of signal-to-noise quality cuts on the original *Gaia* eDR3 parameters. Section 3 describes the cleaning of the sample by gradually introducing further distance cuts to minimize the probability of keeping binaries with long period unseen companions, the use of a RUWE quality cut to exclude unresolved tertiaries, and the implementation of a strict HR diagram selection criteria to isolate only binaries where both components are main-sequence stars with minimal probabilities of including blended

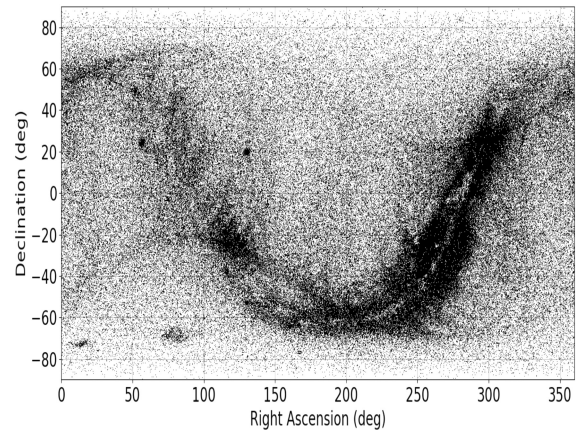


Figure 1. Full sky plot displaying over 800 000 binary pairs from the *Gaia* eDR3 catalogue satisfying our initial search criteria for binary star candidates within 200 pc of the Sun, see text. The presence of nearby groups and associations, as well as heavily crowded fields along the disc of the Milky Way are evident.

tertiaries. In Section 4, we compare our results to those of some similar recent studies. Finally, Section 5 presents our concluding remarks.

2 INITIAL SAMPLE SELECTION

We begin by using the *Gaia* initial search of El-Badry & Rix (2018) who construct a catalogue of wide binaries within 200 pc of the sun, which is then tested through various simulations to account for projection effects, a reasonable distribution of ellipticities and completion due to undetected companions, with a level of contamination estimated by those authors as < 0.2 per cent. An extension of the basic strategy presented in that paper was also used in Tian et al. (2020) to construct a catalogue of over 800 000 wide binaries within 4 kpc of the sun, maintaining a high purity for the sample.

Our initial *Gaia* search returns all stars within 200 pc of the sun having precise parallaxes (signal to noise > 20). The query then scans a projected circle of 0.5 pc about each of these stars for potential companions also required to have fairly precise parallax measurements (signal to noise > 5). Each potential binary pair is then rejected if the parallaxes of the two stars result in a distance difference along the line of sight for the two components larger than twice the projected separation, s , between them, at more than 3σ , i.e. a potential binary pair must satisfy $\Delta d - 2s < 3\sigma_{\Delta d}$. In going to large distances, a growing fraction of close companions will not be detected due to the fixed *Gaia* resolution, our sample is not complete in any volume-limited sense, the requirement is not that we should not miss any valid candidates, but that we should not include invalid ones. This initial search returns close to one million potential binary pairs shown on a sky plot in Fig. 1.

It is clear that a number of well-known local groupings and associations have remained, where wide binaries will not satisfy any strict isolation criterion. Also, crowded regions following the disc of the Milky Way are evident. Next, we demand that if any particular star appears as either the primary or the secondary of more than one potential binary pair, all such potential binary pairs are removed. This results in an isolation sphere of at least 0.5 pc about all of the potential binary pairs passing this criterion, and allows to minimize the effects of possible dynamic perturbations due to other nearby single stars forming part of the average stellar

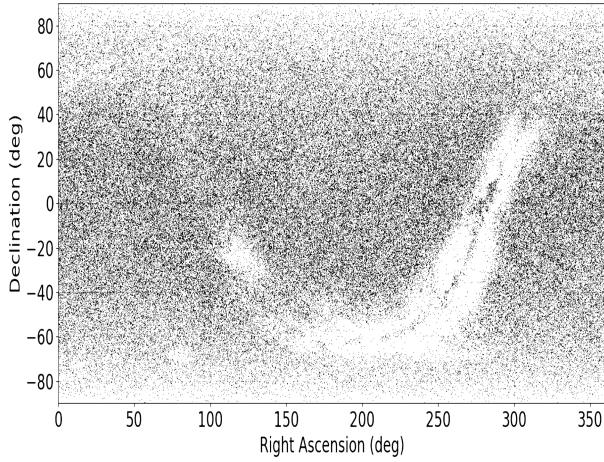


Figure 2. Full sky plot of 169 540 isolated wide binary pair candidates remaining after the removal of all candidate pairs where either the primary or the secondary star had been originally selected as either a primary or a secondary member of more than one binary pair candidate. The remaining binary pairs have no *Gaia* sources with parallax signal to noise determinations >5 within a 3D sphere of 0.5 pc. The removal of all local groups, as well as large areas of crowded fields along the Milky Way disc projection is apparent.

field population. In limiting ourselves to kinematic observations of binaries with projected separations below 0.1 pc, we select stars having no other close neighbours with parallax measurements within at least five times the binary separation; this isolation factor grows linearly in going to closer binaries.

After removing all binaries where either of the two stars forms part of more than one such pair we are left with 169 540 binary pair candidates, shown in a full sky plot in Fig. 2. We can see that the strict cuts applied have removed all evident local groupings, as well as excised the crowded zones along most of the Milky Way disc region.

Before examining the relative velocity distribution of the binary candidates, we will use the relative radial velocities of the two components to minimize the presence of unbound pairs by requiring the difference in radial velocities between both components of each binary to be below 4 km s^{-1} . Thus, we remove from consideration all binary pairs where either component is lacking a radial velocity determination. Also, as pointed out in El-Badry (2019), ignoring detailed spherical geometry correction effects will lead to spuriously inflated (and raising with s) relative velocities for near and wide binaries. Although this correction is only a minor contribution, keeping only stars with radial velocity observations allows the inclusion of full spherical geometry corrections (e.g. Smart 1968) to adequately estimate the true relative velocity of the binaries in our sample. Excluding grouped binaries and those where either component is missing a radial velocity measurement effectively remove over 99 percent of the potential binary candidates. Fig. 3 shows the full sky plot of the 5844 binary pairs remaining, a very significant reduction from the candidate sample of Fig. 2.

We do introduce two modifications to the El-Badry & Rix (2018) query, the first a slight increase in the radius of the projected circle defining the initial search, from the $5 \times 10^4 \text{ au} = 0.25 \text{ pc}$ used by those authors to the 0.5 pc considered here, so as to allow us to explore a somewhat larger range of binary separations. Finally, El-Badry & Rix (2018) introduce a cut in relative velocities on the plane of the sky to exclude any potential binary candidates that are inconsistent with Newtonian dynamics for a $5 M_{\odot}$ total mass binary to 3σ . As

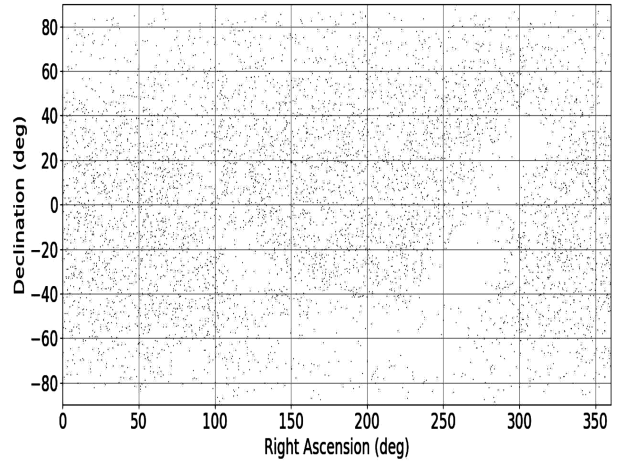


Figure 3. Full sky plot of all 5844 binary pairs in Fig. 2 having radial velocity measurements for both primaries and secondaries.

our aim is to explore precisely the presence of wide binaries showing relative velocities above Newtonian values, we remove this last cut.

Then, we apply strict signal-to-noise (>40) quality cuts to the proper motion measurements in both RA and Dec. for both of the components of each potential binary, in looking for a small sample where all stellar properties used are highly accurate. Only potential binary pairs where both components pass the above data quality cuts in both of their proper motion measurements are retained. In order to minimize the presence of chance associations resulting from random pairs of stars drawn from the local field population, we introduce the cut mentioned previously requiring that the radial velocity difference between the two components of all potential binary pairs must be of less than 4 km s^{-1} , these last cuts leave us with 2868 binary pairs. This relative velocity limit takes the place of the Newtonian consistency criterion in the original query, and ensures that our ΔV inferences will be minimally affected by random fleeting encounters of field stars, which would have velocities each drawn from a Gaussian distribution having a velocity σ of around 40 km s^{-1} , and hence a pairwise velocity difference having also a Gaussian distribution with $\sigma = \sqrt{2} \times 40 \text{ km s}^{-1} \approx 60 \text{ km s}^{-1}$.

Fig. 4 gives the colour–magnitude diagram for this initial sample, dark black points for the 5736 stars from 2868 binaries remaining, with the 169 540 stars from the de-grouped binary pairs, but having no radial velocity measurements shown as the faint grey points. As in all subsequent colour–magnitude diagrams, each binary pair contributes two points, by construction, of the same shade. It is clear that the stars having no radial velocity measurements, are systematically dimmer than the brighter ones where the *Gaia* eDR3 catalogue returns also radial velocities. The former include the dimmer solar neighbourhood main sequence, white dwarfs to the lower left-hand region of the plot, and even a region of white dwarf/main sequence unresolved blended binaries as a diffuse cloud between the main sequence and the white dwarf population.

The main sequence for the selected stars is obvious, as is a band of narrow photometric binaries just above the clear main sequence composed primarily, but not exclusively, of the grey points. Indeed, most photometric binaries do not have radial velocity measurements in *Gaia* as the single star solution fails, providing an extra criterion for excluding such blended cases. As we infer relative velocities on the plane of the sky through proper motion observations over the duration of the *Gaia* eDR3 catalogue, rather than through instantaneous

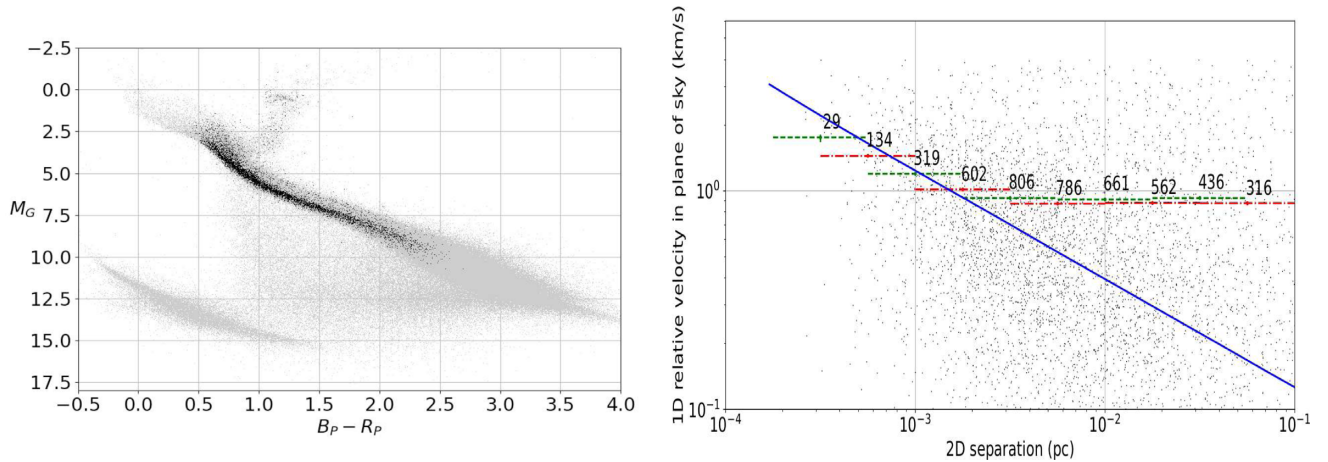


Figure 4. Left(a): Colour–magnitude diagram for all the 5736 stars of the 2868 binary pairs shown in Fig. 3, also having relative radial velocities between both components $<4 \text{ km s}^{-1}$ and signal-to-noise ratio in proper motions for both RA and Dec. for both components >40 , black dots, with the light grey dots showing the 169 540 stars of Fig. 2. The exclusion of white dwarfs, white dwarf/main sequence blends, and the noisier low brightness main sequence is clear. Right(b): Root mean square binned distribution of 1D relative velocities between the members of the 2474 binary pairs shown in the left-hand panel of this figure, which also satisfy having relative velocities in both RA and Dec. $<4 \text{ km s}^{-1}$, and a minimum signal to noise in both of these quantities >0.3 , as a function of 2D projected separations between the members of each binary pair, for RA and Dec. measurements, dashed and dotted lines, respectively, with average relative errors for these two quantities being 10.77 and 11.85, respectively. Each binary pair also appears as a pair of points at a fixed separation, for its corresponding relative velocities in RA and Dec. The solid line gives the Newtonian predictions of Jiang & Tremaine (2010) for this same quantity.

Doppler shift inferences, we are not overly sensitive to either accelerations or velocities induced by hidden tertiaries, only to resulting displacements, which to a varying degree, will be averaged out over the orbit of the hidden tertiaries. Very tight hidden tertiaries with orbital periods much shorter than the 34 month eDR3 *Gaia* mission, lead to high instantaneous velocities, but to very low displacements, which hence imply negligible kinematic contamination through our proper motion relative velocity determinations. Of course, for hidden tertiaries of larger separations, a contamination effect inflating the wide binary relative velocity inference appears, the following section is dedicated to as careful a strategy to minimize hidden tertiaries in our final sample as the current data allow.

We end this section with a kinematic plot for the initial sample in Fig. 4(b), an rms binned distribution of 1D relative velocities as a function of 2D projected binary separation, dashed bins for RA measurements, and dotted for Dec. ones. Further removal of binaries with final relative velocity signal-to-noise values <0.3 or $\Delta V > 4 \text{ km s}^{-1}$ on either RA or Dec. leaves us with 2474 binary pairs having mean signal-to-noise values for RA and Dec. proper motions of 3314 and 3285, and mean signal to noise for parallax measurements of 683. These last two cuts will be also implemented in all of the following kinematic distributions. The mean distance to the Sun for these stars is of 107 pc, and the mean RUWE parameter 1.34. The last low signal-to-noise lower limit on inferred velocities mentioned only excludes a few noisy outliers, the mean signal-to-noise values for this sample are of 10.77 and 11.85 for RA and Dec. velocity inferences, respectively.

As we have ended the sample considered at separations of 0.1 pc, and given the exclusion sphere introduced in the sample selection of 0.5 pc, our binaries included having the largest separations are isolated from any other *Gaia* eDR3 source having parallax measurements out to five times the binary separation. This isolation factor grows to 50 times the binary separation for separations of 0.01 pc, and continues growing linearly towards the smaller separations considered.

The solid line gives the results of Jiang & Tremaine (2010) for the rms 1D relative velocities for a simulated population of 50 000 binary

pairs composed each of two one solar mass stars, and for a random distribution of line-of-sight projections and a reasonable distribution of ellipticities, after 10 Gyr of evolution in the solar neighbourhood under the influence of random encounters with field stars and the influence of the galactic tidal fields, assuming Newtonian gravity. This line closely follows a Keplerian scaling of $\Delta V_{\text{RMS}} \propto s^{-1/2}$ out to the tidal radius of the problem, at close to 0.7 pc, lying beyond the region being explored here. Indeed, we end the figure at a separation of 0.1 pc, which implies that for all the binaries included, both components are at least five times closer than any other *Gaia* eDR3 source from the initial selection. Dim sources having poor parallax measurements can exist within the 0.5 pc projected circle about each of the binary components, but mostly, given our small 200 pc distance cut-off, will be background objects.

We see in Fig. 4(b) kinematics consistent with the Newtonian prediction of Jiang & Tremaine (2010) for the lower separation bins, and a transition to a constant relative velocity distribution for the $s > 1.5 \times 10^{-3}$ region. The faint points in this figure give each individual measurement, as in all subsequent kinematic plots, a small fraction of very small velocity individual points are not displayed as they fall below the range selected to allow a full presentation of the results. The points shown cannot be individually compared to the Newtonian predictions of Jiang & Tremaine (2010) shown, as this prediction refers to the rms values of the resulting distribution of individual points, which is what the numbered binned values given present.¹

¹The rms value for the relative velocities for a large sample of wide binaries modelled under Newtonian gravity and having a distribution of ellipticities and orbital projections with respect to an observer from Jiang & Tremaine (2010), given by the solid line in Fig. 4(b), can only be compared to the rms values of distributions of relative velocities for wide binaries, not to individual values for any particular wide binary. Thus, we give the individual points for the wide binaries obtained to show the full distribution of values we obtain, not as a comparison to the solid line, which can only be meaningfully compared to the binned rms values given. Notice also that the rms value of a distribution is skewed towards large values with respect to the mean, such that if one has a distribution of points appearing equally distributed above

A more careful exploration of the physics behind these trends can be attempted by considering an estimate of the total mass of each binary in this initial sample, and a study of the mass-velocity scalings present. We use the mass estimate in Pittordis & Sutherland (2019) of

$$\left(\frac{M}{M_{\odot}}\right) = 10^{0.0725(4.76 - M_G)}, \quad (1)$$

where the *G*-band *Gaia* absolute magnitude is shown to provide a good stellar mass determination though the above equation, for main-sequence stars. Power-law fits to binned distributions of average ΔV as a function of binary mass for the data shown in Fig. 4(b) yield logarithmic slopes of 0.33 ± 0.12 and 0.32 ± 0.07 for the $s < 1.5 \times 10^{-3}$ and $s > 1.5 \times 10^{-3}$ regions, respectively. The lack of a clear $\Delta V \propto M_b^{0.5}$ scaling in the $s < 1.5 \times 10^{-3}$ region probably indicates the presence of significant kinematic contamination in our initial sample, as evident, for example, in the presence of a few spectroscopic binaries in the black points of Fig. 4(a). Also, the consistency of the two mass-velocity scalings mentioned above suggests a common origin for the relative velocities shown, again probably dominated by kinematic contaminants. Further cleaning of the sample to minimize the presence of the above and other sources of kinematic contamination is described in the following section.

3 CLEARING KINEMATIC CONTAMINANTS

In this section, we describe a sequence of three further data quality and kinematic contaminant exclusion criteria, which will be applied sequentially, such that at any point, all previous criteria are also present. The first step towards eliminating kinematic contaminants consists of introducing a distance cut-off to restrict our sample to a smaller, higher quality set where the prevalence of undetected stellar companions diminish, as all apparent magnitude-dependent systematics are reduced. Of course, any restriction in the maximum distance considered implies a trade-off in terms of a fast drop in the number of remaining binary pairs. We find that the most restrictive distance cut-off that still yields a workable number of binary pairs is 130 pc. This further restriction leaves us with 1850 binary pairs, the 3700 stars shown in the colour–magnitude diagram of Fig. 5(a), with the background light grey points being the same as the ones shown in Fig. 4(a).

The corresponding kinematic plot is presented in Fig. 5(b), where after exclusion of low-velocity signal-to-noise pairs and imposing a maximum relative velocity on the plane of the sky of 4 km s^{-1} , as described in the case of Fig. 4(b), we are left with 1642 binary pairs. The mean distance, mean signal to noise in RA and Dec. and mean RUWE values of this sample are of 79.6 pc, 4,091, 4,047, and 1.37, respectively. We see the reduction in the distance resulting in more accurate astrometric observations.

Comparing the colour–magnitude diagrams of Fig. 5(a) to Fig. 4(a), we see that the reduction in the distance significantly reduced the number of photometric binaries in the sample in the distinct band just above the main sequence, which also appears more clearly defined. Brighter stars in the turn-off region are also diminished, as the total numbers dropped. In comparing Figs 4(b) and 5(b), we see that the distance reduction and corresponding kinematic cleaning of the sample resulted in a slight drop in the amplitude of the constant ΔV_{RMS} region to the right of the plot, but no significant qualitative changes. Indeed, the mass-velocity scalings

for both the region following the Newtonian predictions of Jiang & Tremaine (2010), and the one to the right of this presenting the slight drop in amplitude described above, show again power-law fits with logarithmic slopes consistent with those of Fig. 4(b), and not corresponding to any evident physical scalings.

The next quality cut introduced is to directly limit the maximum of the allowed RUWE parameters for the stars considered. This parameter gives a measure of the goodness of fit for the *Gaia* single star solution performed on each of the sources modelled, and is known to shift to larger values in cases where unresolved stellar companions are present, e.g. Belokurov et al. (2020). We introduce an upper cut-off RUWE < 1.2 such that if either the primary or the secondary of a given binary pair fails this test, the binary pair is removed from the catalogue. Comparing to the mean RUWE parameters of the samples displayed in Figs 4 and 5, of 1.34 and 1.37, it is clear that the upper limit introduced at this stage presents a fairly large cut.

In fact, the black points in the colour–magnitude diagram of Fig. 6(a) represent only the 2016 stars from 1008 binary pairs showing an extremely well-defined main-sequence region with practically no evident photometric binaries above it. Also, the turn-off region is now almost empty, as is also the case for the main sequence to the right of a colour of about 2.25, where larger errors, and hence higher probabilities of contamination from unresolved stellar companions, are evident from the underlying light grey distribution.

Fig. 6(b) gives the kinematic plot for this sample, which contains only 929 pairs of wide binaries having very high quality *Gaia* fits for both components, indeed, the mean RUWE values this time are of only 0.99. As a reflection of having a much cleaner sample than we started with, the mean signal-to-noise values for proper motion observations in RA and Dec., and parallax are now 4123, 4073, and 911. This time we see a more pronounced change with respect to the previous Figs 4(b) and 5(b), in that the region over which our results trace carefully the Newtonian predictions of Jiang & Tremaine (2010) now extends to larger separations, with results being consistent with it out to close to 10^{-2} pc. Concurrently, the amplitude of the constant ΔV_{RMS} region has again dropped and now appears at about 0.5 km s^{-1} . Although the total numbers have dropped considerably from the 2474 binaries of Fig. 4(b), due to the removal of binary candidates where the probabilities of kinematic contamination were much higher than for the remaining ones, the very small dynamical range in the total masses, of only about a factor of 2.2, still does not allow a clear detection of any physically significant mass velocity trend, over any of the regions in this diagram.

We now turn to the final pruning of our catalogue where we select directly on the colour–magnitude diagram for regions containing minimal presence of unresolved stellar companions, after all the cuts described previously have been sequentially applied. Belokurov et al. (2020) present an extremely detailed analysis of binarity, variability, and kinematic contamination on wide binary relative velocities as a function of RUWE parameter and location in the colour–magnitude diagram of the *Gaia* catalogue. Using their results, we define a narrow region of the upper main sequence as the final inclusion criteria. The region selected, morphologically through M_G and $B_p - R_p$ ranges, in addition to our previous RUWE filter, limits the presence of any kinematic contaminants through unresolved stellar companions to less than 5 per cent, according to the results of Belokurov et al. (2020), e.g. their fig. 10 right for the magnitude range we use here. Indeed, even the presence of hot or outer Jupiters can be constrained to fall rapidly for stars with RUWE indices below 1.0. As with all our previous cuts, all binaries for which either the primary or the secondary fail the colour–magnitude selection criteria are removed.

and below a prediction for an rms value, the distribution being considered will necessarily have an rms value larger than the prediction in question.

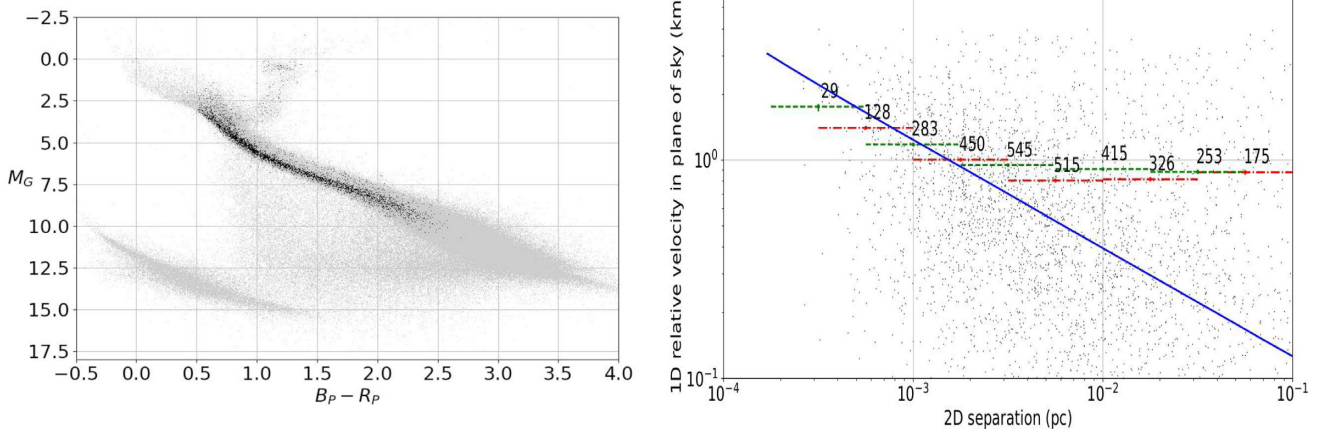


Figure 5. Left(a): The figure is analogous to the left-hand panel of Fig. 4, but contains only as the black points the 3700 stars from the 1850 binary pairs remaining after the further inclusion of a distance cut of 130 pc from the sun, resulting in a significant reduction in the numbers of photometric binaries. Right(b): The figure is analogous to the right-hand panel of Fig. 4, but this time contains only 1642 binary pairs, after the distance cut described above. Average relative errors for right ascension and declination velocity differences are of 13.17 and 15.01, respectively.

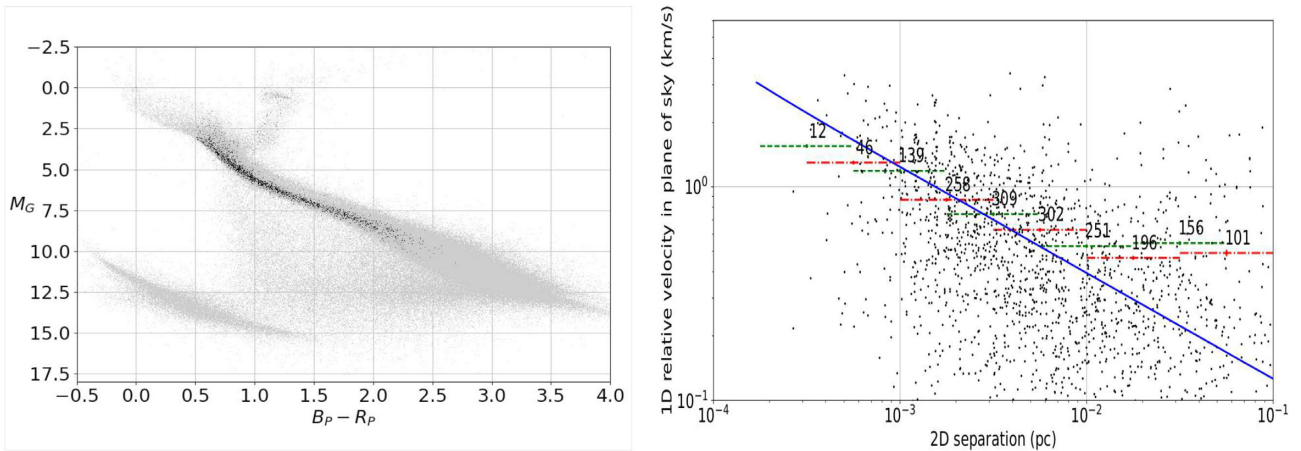


Figure 6. Left(a): The figure is analogous to the left-hand panel of Fig. 5, but contains only as black points 2016 stars from the 1030 binary pairs after the further inclusion of a $\text{RUWE} < 1.2$ cut, resulting in an almost complete exclusion of photometric binaries and a significant reduction in the number of post turn-off stars. Right(b): The figure is analogous to the right-hand panel of Fig. 5, but this time contains only 929 binary pairs, after the data quality cut described. Average relative errors for right ascension and declination velocity differences are of 14.39 and 15.88, respectively.

Our inclusion region in the colour–magnitude plot is shown in Fig. 7(a), and comprises only a very well-defined section of the upper main sequence. This region is defined as all stars within a ± 0.4 vertical magnitude interval of the line joining points (0.7, 4.7) and (2.0, 8.7), where the numbers give magnitude, colour coordinates. This final selection leaves only 444 binary pairs, which after the kinematic signal to noise and upper relative velocity criteria of 4 km s^{-1} , results in the 423 binary pairs appearing in Fig. 7(b). For this final high-quality sample the average signal-to-noise values for the *Gaia* input parameters used are now of 4202, 4064, and 950 for RA and Dec. proper motions, and parallaxes, respectively. The final average relative velocity signal-to-noise values for this sample are about 50 per cent higher than those of the initial sample of Fig. 4, 14.88 and 18.62 for RA and Dec., respectively.

This final kinematic plot is largely consistent with the previous one of Fig. 6(b), with the amplitude of the region showing no dependence of the ΔV_{RMS} values on separation still at 0.5 km s^{-1} . Also evident is the appearance of random fluctuations indicative of shot noise beginning to become relevant as the numbers of binary

pairs considered have continued to fall. The region of consistency with Newtonian predictions now extends to about 10^{-2} pc .

Finally, we present in Fig. 8(a) the mass-velocity scaling for the 295 binary pairs having separations below 0.009 pc in Fig. 7(b), and the 128 such pairs with separations larger than 0.009 pc also from Fig. 7(b), in Fig. 8b. It is interesting that despite the very narrow dynamical range allowed by intrinsic stellar physics and the low numbers remaining after the very strict series of cuts applied, Fig. 8(a) shows a scaling of mean 1D velocity differences for the selected binaries of $\Delta V \propto M_b^{0.52 \pm 0.14}$ (with a correlation coefficient of 0.88, much higher than that of any previous mass-velocity scalings), perfectly consistent with Newtonian expectations, which indeed are clearly met as apparent in the $\Delta V_{\text{RMS}} \propto s^{-1/2}$ scaling shown in Fig. 7 (b) for this region. This last result validates the procedure undertaken aiming at identifying an extremely high quality and high purity catalogue of isolated solar neighbourhood wide binaries, albeit including only small numbers of such stellar pairs.

Our final plot shows the mass velocity scaling for the 128 wide binary pairs having $s > 0.009 \text{ pc}$ in Fig. 7(b). The average binary mass

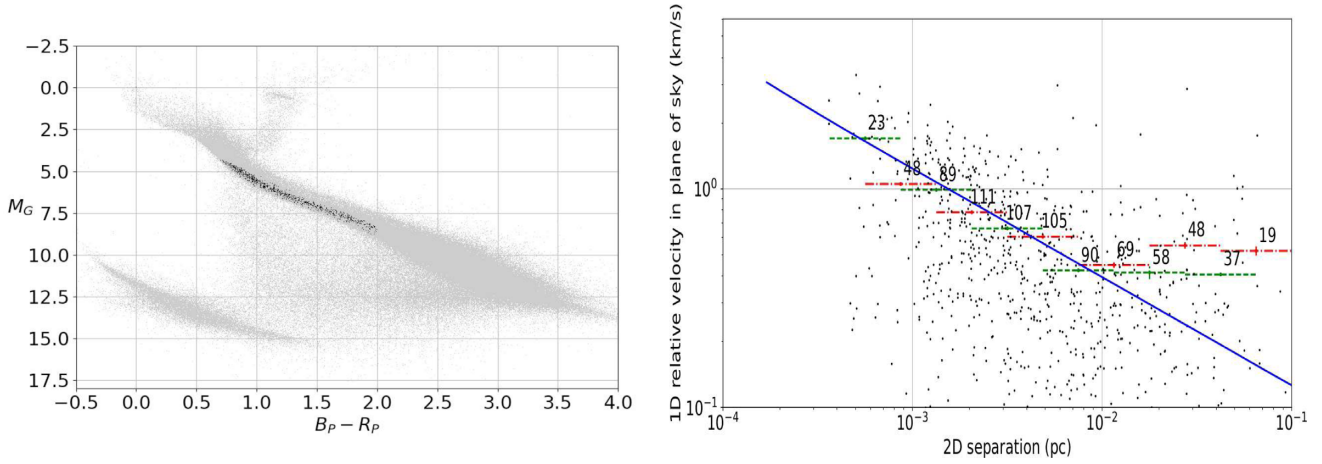


Figure 7. Left(a): The figure is analogous to the left-hand panel of Fig. 6, but contains only as black points 888 stars from the 444 binary pairs after the further inclusion of a strict colour–magnitude selection, as shown in this figure, restricting the sample to the cleanest region identified by Belokurov et al. (2020) in terms of near absence of any kinematic contaminants. Any binary pair where either component falls outside the selected region is removed. Right(b): The figure is analogous to the right-hand panel of Fig. 5, but this time contains only 423 binary pairs, after the data quality cut described. Average relative errors for right ascension and declination velocity differences are of 14.88 and 18.62, respectively.

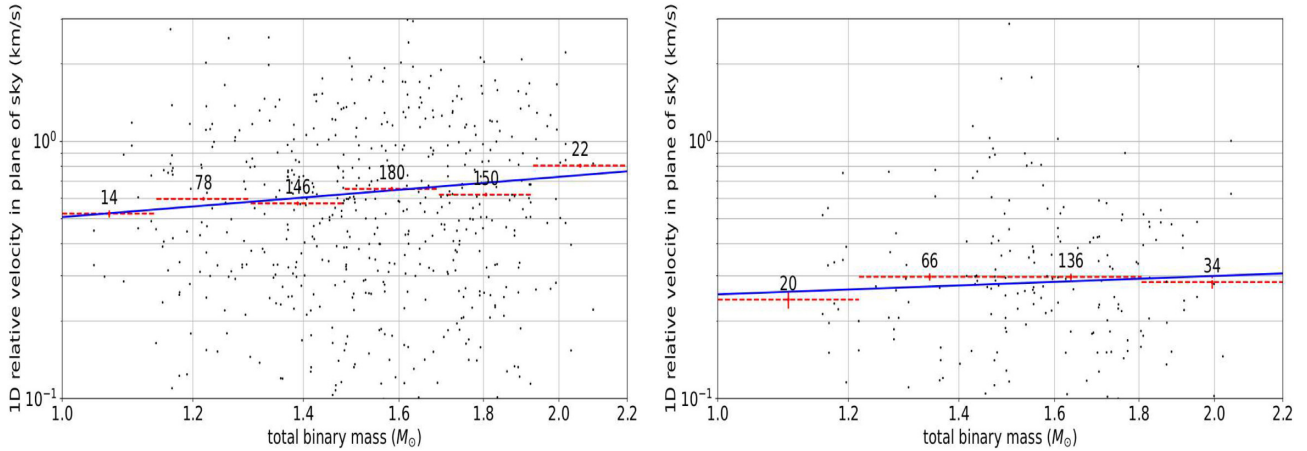


Figure 8. Left(a): This panel shows the binned average 1D relative velocity versus binary mass scaling for the binaries with separations < 0.009 pc in the right-hand panel of Fig. 7, where each binary pair contributes two points, one for RA and one for Dec. observations. Average relative errors for right ascension and declination velocity differences are of 18.36 and 23.56, respectively. A power-law fit to this scaling yields $\Delta V \propto M_b^{0.52 \pm 0.14}$. Right(b): This panel is analogous to the left one of this figure, but for separations > 0.009 pc. Average relative errors for right ascension and declination velocity differences are of 6.85 and 7.24, respectively. A power-law fit to this scaling yields $\Delta V \propto M_b^{0.24 \pm 0.21}$.

for this last plot is of $1.6 M_\odot$, as it is also the case for Fig. 8(a). The scaling in this final plot is of $\Delta V \propto M_b^{0.24 \pm 0.21}$, with a correlation coefficient for these small numbers of stars of 0.63. As with the previous plot, we have divided the full mass range into as many bins as permitted by the constraint of having at least 10 data points in each bin. The *Gaia* eDR3 identifiers and relevant parameters used for these 128 wide binary pairs appear in the appendix.

We caution that the confidence intervals quoted for the mass velocity scalings in all cases are lower limits to this quantities, as they are only formal statistical ranges which ignore a series of statistic and systematic errors still present. One of the above is the variance inherent to the stellar mass estimates of equation (1), which are hard to estimate. In the similar magnitude, colour mass estimate through isochrone comparisons of El-Badry & Rix (2018), a confidence interval of $\pm 0.1 M_\odot$ for their photometric mass estimates, which closely match those of equation (1) for the main-sequence range we use, is given.

Also, given the small numbers of binary pairs available in Fig. 8(b), the shallow velocity mass scaling present and the narrow M_b dynamical range accessible, the slope obtained is sensitive, to within about 1.5 times the quoted confidence interval, to details of the various data quality cuts and kinematic contamination cleaning procedures applied. Still, there is a clear indication for a lower slope for the velocity mass scaling in the $s > 0.009$ pc region compared to the one found in the $s < 0.009$ pc one, which is in fact consistent with the $V_{TF} = 0.35(M/M_\odot)^{1/4} \text{ km s}^{-1}$ galactic $a < a_0$ Tully–Fisher scaling.

To summarize, hidden tertiaries with bright companions are effectively photometric binaries, which are efficiently excluded through the HR diagram selection, as well as through their lack of accurate single stellar photometric and spectroscopic solutions, evident through large values of the RUWE parameter and lack of reported radial velocities, respectively. Hidden tertiaries with dim companions and separations lower than about 10 au induce a

wobble on the detected member of the large-scale binary, which results in poor *Gaia* single stellar fits, and hence can be largely excluded through RUWE parameter upper limits. On this point, Belokurov et al. (2020) estimate less than 5 per cent hidden tertiaries contamination for internal separations below 10 au, on the HR region of interest, for a RUWE upper limit of 1.4, for stars within 1 kpc of the sun. These numbers can be compared to the much stricter upper RUWE cut-off 1.2 (and final average values of 0.99) and distance limit of 130 pc that we impose on our final sample. Hidden tertiaries with internal separations between about 10 and 100 au will be hard to exclude, although their frequency will drop as the distance limit of our sample is reduced. Even assuming all of these appear in our sample, from empirical estimates of tertiary stellar systems (e.g. a total fraction of 40 per cent from Tokovinin et al. 2002, 2010) we can expect less than about a 15 per cent contamination in our final sample, for equally populated logarithmic separation intervals, e.g. Clarke (2020). These systems would result in artificially enlarged relative velocities of $\lesssim 1 \text{ km s}^{-1}$ on the small fraction of affected binaries. Finally, unbound flybys are restricted through the use of a relative radial velocity filter of $< 4 \text{ km s}^{-1}$, a relative velocity on the plane of the sky filter also of $< 4 \text{ km s}^{-1}$, and the careful de-grouping procedure that ensures only isolated binaries remain in our final sample. Given the mean average interstellar distance of 1 pc in the solar neighbourhood, and the pairwise velocity dispersion of about 60 km s^{-1} for these stars, the presence of unbound flybys in our final sample of wide binaries with separations below 0.1 pc, is extremely unlikely.

Throughout this project we used *Bynary*, a suite of PYTHON programs that easily downloads stellar and binary data from *Gaia*, filters and processes them via its colour–magnitude, kinematic, and velocity/mass modules to produce the graphs and statistics presented here, also allowing the user either to export data for other analysis programs and purposes or looking at the corresponding entries of any relevant binary pair in a range of possible surveys (e.g. DSS, 2MASS, ALLWISE, GALEX, *Fermi*, or IRIS). A full description and release of *Bynary* will be the subject of a future publication.

4 COMPARISON TO PREVIOUS RESULTS

We now present a comparison of our results to a series of recent similar studies, focusing on the degree to which these are consistent with our current findings and the differences in sample selection criteria, data quality available and assumptions made when interpreting the results obtained.

4.1 Hernandez et al. (2019a)

In Hernandez et al. (2019a) the data were much scarcer, as the authors started from a *Hipparcos* wide binary selection sample by Shaya & Olling (2011), leaving only 81 binaries in the final sample (in part due to the 1/3 missing *Hipparcos* sources in DR1), with projected separations between 0.003 and 10 pc, allowing for only two bins below 0.1 pc. Thus, having one bin at close to 0.04 pc showing a clear deviation from Newtonian expectations and one slightly below 0.01 where the large error bars made it ambiguous in terms of following or not the Newtonian prediction, identified the region between 0.001 and 0.1 as crucial for detailed analysis. Fig. 5 in Hernandez et al. (2019a) does not allow more than an order-of-magnitude identification of the threshold beyond which deviations from the Newtonian prediction appear, given the very limited number of bins and the large error bars resulting from the small numbers of binaries available in that study.

Also, the large separations sampled in that study become suspicious in terms of external perturbations, given the average interstellar separations of close to 1 pc in the solar neighbourhood, the possibility of substantial kinematic contamination due to interactions with surrounding stars becomes a worry beyond a few tenths of a pc. Extending the binary separation range explored to close to 1 pc and beyond is problematic not only in terms of excluding external kinematic perturbations but also as binary identification becomes ambiguous, within the 1 pc typical interstellar separation of the average distribution.

For the above, we decided here to concentrate on an extremely clean sample of isolated binaries where an exclusion sphere many times larger than the binary separation could be defined about each, as detailed in the sample selection section, and with significant resolution in the separation interval between 0.001 and 0.1 pc. These permit a clear tracing of the Newtonian region, which serves as a control of the whole procedure in as much as an accurate agreement with the Jiang and Tremaine (2010) predictions is recovered, and a more accurate identification of any divergence occurring, within a regime highly free from contamination due to the average field star distribution.

Given the small number of bins and much larger error bars in Hernandez et al. (2019b), our present results are consistent with those previous findings, to within the significantly extended confidence intervals of that previous study.

4.2 Clarke (2020)

The highly relevant recent work of Clarke (2020) showed that the presence of blended tertiaries, cases where one or both of the two components of an observed binary are in fact small-scale binaries themselves containing an undetected component, will result in kinematic contamination inflating the inferred relative velocities of the observed large-scale binary. That study shows that a distribution of reasonable separations and masses of blended tertiary components with a high hidden tertiary fraction of 0.5, can be invoked to fully account for the results of Hernandez et al. (2019b). It is interesting that such a distribution of undetected tertiaries should become apparent through a variety of effects.

However, the results of Clarke (2020) depend critically on the details of the assumed distribution functions. There, the separation distribution of hidden tertiaries is assumed as uniformly distributed in log separation between 3 and 100 au. This means that a fraction of 0.343 of the hidden tertiaries in that study lie in the 3–10 au interval. This first inner separation interval is the one producing the greatest effect on the resulting wide binary relative velocities inferences in the context of Clarke (2020), as it is the closest of the hidden tertiaries that have the largest kinematic contamination effects on the large scale wide binary, given the Newtonian $r^{-1/2}$ scaling for velocities with separation, and as all equal logarithmic intervals were assumed there as equally populated. As Clarke (2020) acknowledges, many of the hidden tertiaries assumed in that study would imply anomalies in their location in the HR diagram, as well as astrometric solutions of degraded quality, all of which allows to remove from consideration such affected binaries. It is because of the result-defining effect blended tertiaries could have on our analysis, that we have gone through an extremely thorough cleansing process, guided by the Clarke (2020) results, and the Belokurov et al. (2020) criteria.

In that last paper, through careful and extensive simulations within *Gaia* DR2 parameters and comparisons with observations from *Gaia* DR2, it is concluded that close hidden tertiaries with separations

below 10 au can be detected mostly through the RUWE flag, and also in combination with taking nearby samples with high quality astrometric solutions, i.e. high signal-to-noise values in parallax and proper motions, see also Penoyre et al. (2020). Taken together, the conclusion of the two above papers is that with a RUWE filter of 1.4 and high signal-to-noise cuts for nearby samples, together with HR selection criteria as we have applied, one can exclude hidden tertiaries to below a 5 per cent contamination level, see e.g. the upper row in fig. 9 of Belokurov et al. (2020) for the hidden tertiary fraction for main-sequence stars in the magnitude range we select. This excludes the 3–10 au separation interval, which is crucial for the Clarke (2020) result. Further, it is important to note that the Belokurov et al. (2020) result is valid for the 22 month *Gaia* DR2 duration, the 1.55 times larger 34 month eDR3 time interval, at comparable data quality, translates into a $1.55^{2/3} = 1.34$ larger separation exclusion of 13.4 au. Thus, the original $\log(100/3) = 1.523$ logarithmic interval assumed in Clarke (2020) should be reduced to a $\log(100/13.4) = 0.873$ interval, i.e. an interval smaller by a factor of 1.75, which crucially, is missing the inner 3–13.4 au separation range. Thus, in going from DR2 to eDR3, and taking all precautions derived from the results of Belokurov et al. (2020) and Penoyre et al. (2020) we can be confident that close to half of the hidden tertiaries assumed by Clarke (2020) to reproduce the non-Newtonian high relative velocity distribution, indeed, the most relevant half, as the kinematic contamination effects of hidden tertiaries will scale with separation as $s^{-1/2}$, are not valid as an assumption in our present data and experimental set-up to explain the results obtained at large separations.

Notice also that we have adopted a much more strict (in terms of the fraction of *Gaia* systems remaining) RUWE cut-off 1.2, compared to the fiducial value of 1.4 explored in Belokurov et al. (2020) as a reference limit below which hidden tertiaries with separations below 10 au can be largely excluded (for distances of up to 1 kpc, much larger than the high quality limit of only 130 pc that we impose), and that the average RUWE for our final sample is of a very stringent 0.99. It is clear that the hidden tertiary separation interval allowed by our present set-up 13.4–100 au, would require significantly more than twice the hidden tertiary fraction assumed by Clarke (2020) to explain the high relative velocity distribution found above Newtonian expectations. As this assumed fraction in Clarke (2020) was actually of 0.5, already in the high end of empirical estimates [e.g. of between 22 per cent and 36 per cent per binary in Tokovinin et al. (2002, 2010), with no evidence of any separation dependence for this fraction], explaining our present results through the Clarke (2020) argument would not be possible even if one assumes a limiting fraction of hidden tertiaries of 1.

4.3 Pittordis & Sutherland (2019)

Using *Gaia* DR2, Pittordis & Sutherland (2019) examine the distribution of relative velocities between the components of wide binaries, for four binary separation intervals between 0.025 and 0.1 pc. Thus, they sample the region where we find a clear signal above Newtonian expectations. Just like in this study, these authors find a clear signal for relative velocities above Newtonian expectations, in an extended relative velocity distribution for all their separation bins sampled, which they mention probably corresponds to the non-Newtonian signal reported in Hernandez et al. (2019b), and which corresponds to the kinematic signal modelled by Clarke (2020) as arising from hidden tertiaries. These authors, however, model the full distribution of relative velocities obtained as the sum of Newtonian expectations and an extra distribution made up of whatever does not conform to Newtonian expectations, which they assign to flybys, unbound

transient pairs that happen to present projected separations in the sampled range, without there being any physical association between them. As these authors did not calculate the mass velocity scaling within this extended tail, it is hard to see if our results are also consistent in this more physical sense, as well as in terms of the presence of a non-Newtonian high relative velocity extension.

As the authors acknowledge in Pittordis & Sutherland (2019), the flyby interpretation of the non-Newtonian high relative velocity remainder to their full distribution once the Newtonian component has been removed, is actually inconsistent with the expected behaviour of any such flybys. Whilst even in their simulations (as expected under any reasonable modelling of a flyby population) the fraction of flyby systems increases as the binary separation range increases, due to the larger cross-section for the flyby, their fits to flyby fractions once the purely Newtonian contribution is subtracted from their observations, require always diminishing flyby fractions as binary separations increase. It is not only the behaviour of the flyby fraction that is inconsistent, but also the velocity distribution. As explained previously, if relative velocities are drawn at random from the Gaussian field distribution of velocities, with a velocity dispersion close to $\sigma = 40 \text{ km s}^{-1}$, the expected pairwise velocity will also have a Gaussian distribution, with a velocity dispersion $\sqrt{2}$ times larger, and hence, for the $\approx 1 \text{ km s}^{-1}$ relative velocities observed for the wide binaries in question, the flyby distribution would have a very close to constant velocity distribution, and not the elaborate distributions peaked before Newtonian values and slowly falling thereafter required by these authors once the data are split between a Newtonian compliant set and an everything else remainder. Further, given the typical interstellar separations of 1 pc, flyby fractions of order 0.5, as required by the authors in question, at binary separations of a few hundredths of a pc, appear unlikely.

Thus, there is not any evident inconsistency between our current results and those of Pittordis & Sutherland (2019), rather, a clear distinct interpretation of the results. We are merely presenting empirical data which resemble Tully–Fisher dynamics in the same general acceleration range as relevant for the galactic case (in both separation versus velocity and mass versus velocity scalings), without hazarding any detailed interpretation. Additionally, in this study we are using *Gaia* eDR3 data, where typical proper motion errors have gone down by a factor of 2 with respect to the DR2 data used by Pittordis & Sutherland (2019), it is therefore entirely possible that a number of systems which they could accommodate within a Newtonian distribution within the errors, would now have to be assigned to the peculiar flyby high-velocity tail.

5 DISCUSSION

Whilst it is impossible to be certain that no kinematic contaminants remain in our final sample, the thorough pruning strategy undertaken, aimed at producing very high quality if small samples, together with the convergence of our results seen in Figs 6(b) and 7(b), strongly suggest an intrinsic origin to the asymptotically flat relative velocity signal obtained towards large separations in our final sample. The study of the internal kinematics of $s > 7000 \text{ au}$ binaries is still a very recent field, where significant observational and theoretic studies are in all probability yet to come. In attempting to reconcile our still incomplete present data to either Newtonian or MONDian expectations, we find that both paradigms present problems, as we discuss below.

Within a Newtonian framework, this result is troublesome for a number of reasons. First, we should expect to see a substantial population of wide binaries with separations larger than 10^{-2} pc

showing kinematics consistent with Newtonian expectations, much below the signal we detect. This signal shows no dependence on the separation and has a constant rms value consistent with 0.5 km s^{-1} between 10^{-2} and 10^{-1} pc. Wide binaries in the above separation range, well within the Newtonian tidal radius of ≈ 0.7 pc, following Keplerian kinematics appear only in very reduced numbers in our *Gaia* eDR3 sample.

Secondly, it is hard to explain the presence of a clearly defined population of wide binaries in the above separation range with relative velocities in the plane of the sky having rms values consistent with 0.5 km s^{-1} . If these binaries are unbound interlopers, the lifetime of such systems for the middle of the above range of 5×10^{-2} pc is a mere $(5 \times 10^{-2}/0.5) \times 10^6 \approx 10^5$ yr. Thus, given the lifetimes of the stars involved of close to 10 Gyr, the wide binaries defining the signal we find with rms relative velocity values of close to 0.5 km s^{-1} would have to be interpreted as fleeting transients lasting only of the order of 10^{-5} times the lifetimes of the stars involved.

Despite the thorough kinematic contamination removal strategy undertaken, we do expect the presence of a remaining fraction close to 40 per cent of hidden tertiaries in the separation interval 13.4–100 au, (resulting in close to one in every 7 of our final binaries, if we assume the constant distribution of hidden tertiaries per logarithmic interval of Clarke 2020), as per empirical estimates in Tokovinin (2002) and (2010). For example, a $0.3 M_{\odot}$ hidden tertiary orbiting at 100 au from one member of a Newtonian wide binary composed of two $1 M_{\odot}$ stars, would modify the relative velocity of the binary in question, from 0.2 km s^{-1} in the absence of the hidden tertiary, to up to about 1 km s^{-1} , depending on the relative orientations of both orbits and ellipticity. However, it appears unlikely that any remaining kinematic contaminants, hidden tertiaries or flybys, should constitute a dominant kinematic contamination effect, for the reason explained below.

If hidden tertiary contamination were a dominant factor in the non-Newtonian separation region of our final plot, to the right of 0.009 in Fig. 7(b), and given the empirical absence of a correlation between tertiary fraction and wide binary separation (e.g. see Tokovinin et al. 2010), such a contaminant would be equally present throughout the Newtonian region. Towards the small separations, it would clearly be of a very minor relative amplitude, but it would be equally dominant kinematically just to the left of the transition between both regimes. We have checked that the clear Newtonian consistent scaling we report in Fig. 8(a) for the Newtonian region of Fig. 7(b) is not lost in going to the larger separations within this regime. In fact, for the 0.003–0.009 pc separation range in Fig. 7(a), we obtain a mass-velocity scaling of $\overline{\Delta V} \propto M_b^{0.56 \pm 0.28}$ with a correlation coefficient of 0.71. The uncertainty in the slope is now somewhat larger than what we obtain for the much more populated 0.0004–0.009 range in Fig. 7(b) of $\overline{\Delta V} \propto M_b^{0.52 \pm 0.14}$, but crucially, remains with Newtonian expectations of 0.5, to well within the confidence intervals.

If kinematic contaminants were dominant for separations above 0.009 pc, they would be equally dominant just to the left of this value, and then we should expect a constant mass-velocity scaling across the transition. This is not what happens, as to the right of 0.009 pc the mass-velocity scaling shifts to a much smaller $\overline{\Delta V} \propto M_b^{0.24 \pm 0.21}$. The use of the mass-velocity scalings in the various regions of the plots presented, furnishes an independent physical diagnostic into the likely causes of the trends seen in the velocity-separation plots. The clear Newtonian mass-velocity scaling obtained for both the entire separation range showing a Newtonian velocity-separation scaling in Fig. 7(b) and the small 0.003–0.009 region immediately preceding the divergence from Newtonian expectations, is an indication of the fact that any remaining level of kinematic contamination is

not a dominant contribution, across the entire Newtonian and non-Newtonian regions.

On the other hand, if they are transients, they are also inconsistent with being chance wide encounters of pairs of stars being drawn from the average Milky Way stellar velocity distribution at the solar neighbourhood. As pointed out previously, the distribution of relative velocities of pairs will be a Gaussian having a velocity dispersion of close to 60 km s^{-1} . Given the upper kinematic cut-off of 4 km s^{-1} we introduced, much smaller than the pairwise relative velocity dispersion for stars drawn from the overall solar neighbourhood distribution, we should expect a close to constant distribution of relative velocities for the binaries we study, uniformly distributed between 0 and 4 km s^{-1} . Such a distribution of relative velocities would have an rms value slightly above 2 km s^{-1} , much higher than the 0.5 km s^{-1} we obtain, and inconsistent with this value at many times the statistical errors of the extremely high quality *Gaia* eDR3 catalogue.

Thus, random stars in the solar neighbourhood that just happen to find themselves within a distance of 5×10^{-2} pc of each other, would necessarily show relative velocities much higher than those we find. Further, the average interstellar separation at the solar neighbourhood of about 1 pc, makes the stars having separations of between 10^{-2} and 10^{-1} pc and relative velocities close to 0.5 km s^{-1} , inconsistent both with Newtonian bound binaries, and chance passing encounters within the solar neighbourhood.

If the results we obtained are due to a population of bound wide binaries that display kinematics inconsistent with Newtonian dynamics, a few first-order estimates become illustrative. First, it is interesting to note that the critical separation beyond which the observed kinematics cease to follow the Newtonian predictions of Jiang & Tremaine (2010) is only slightly below, considering the accuracy allowed by the bin size imposed by the numbers of binaries in our final plot, a value of 0.035 pc. This being the threshold originally identified in Hernandez et al. (2012a) as the limit separation beyond which a binary system composed of $1 M_{\odot}$ stars will find itself in the low acceleration $a < a_0$ regime, where gravitational anomalies frequently identified as signalling the presence of dark matter haloes in the context of galactic dynamics appear (e.g. Milgrom 1983 or Lelli et al. 2017).

Also, the transition appearing at the above-mentioned threshold, is reminiscent of the one between an inner baryonic-dominated regime in galaxies, and the subsequent $a < a_0$ flat rotation curve region, in that what we find is precisely such a Newtonian consistent baryonic small separation regime, which transitions to a constant relative velocity region that would imply, under a Newtonian scenario, the presence of a singular isothermal dark matter halo. At the length and velocity scales being probed, such a dominant dark matter halo around all stars would be inconsistent not only with standard structure formation scenarios but also with the total mass budget of the Milky Way disc, e.g. Kuijken & Gilmore (1991).

Finally, it would appear as an unlikely coincidence, in the absence of a causal connection, that if one extrapolates the baryonic Tully–Fisher relation between the total baryonic mass of a galaxy and the amplitude of its rotation curve, $V_{\text{TF}} = 0.35(M/M_{\odot})^{1/4}$ down to stellar mass scales, e.g. the $1.6 M_{\odot}$ average binary masses we infer for the main sequence stars examined in Fig. 8(b), one should obtain for the corresponding flat rotation amplitude, a value of 0.4 km s^{-1} . This last is remarkably close to the rms relative velocity on the plane of the sky that we obtain for the ‘flat rotation’ separation region, of $\approx 0.5 \text{ km s}^{-1}$.

Within a purely Newtonian scenario, the possibility of very low luminosity undetected tertiary or higher hierarchy companions can

of course not be ruled out, extremely cold white dwarfs, or even black holes with periods longer than the *Gaia* temporal baseline will not produce a significant wobble (Belokurov et al. 2020) of the type the presence of which we can infer through a decrease in the goodness of fit as evident through increasing RUWE indices. This form of dark matter would of course be an *ad hoc* solution which one would have to introduce coincidentally on crossing the $a < a_0$ threshold, and of just the right amplitude to essentially match the Tully–Fisher extrapolation mentioned above.

On the other hand, our results cannot be reconciled with MOND in a straightforward way either. This is because in the most well studied versions of MOND one expects the appearance of an external field effect, such that if a system is internally in the low-acceleration regime, but embedded within a $a > a_0$ or $a \approx a_0$ larger system, like the wide binaries we study here which form part of the solar neighbourhood of the Milky Way, the modifications with respect to Newtonian predictions are expected to be very small, of the order of a 20 per cent effect, e.g. Pittordis & Sutherland (2019). Although MOND is a fundamentally empirical construction, the external field effect remains mostly a prediction, albeit recent claims of a detection in the specific context of statistical studies of rotation curves of spiral galaxies, e.g. Haghi et al. (2016) and Chae et al. (2020b).

In the absence of a definitive covariant version of MOND, it is entirely possible that a low-velocity limit for a finished theory might appear where the external field effect is absent (as in e.g. Milgrom 2011), or that such an effect might have mass or scale dependences different from what results in current well-studied versions of MOND. Many modified gravity theories having a low velocity MOND limit have also been proposed (see e.g. the very incomplete list given in the introduction) where the details, or even existence of the external field effect, have yet to be explored.

Beyond any theoretical interpretation, the results presented here suggest a ‘baryonic Tully–Fisher’ phenomenology at stellar scales, which undoubtedly warrants further investigation, awaiting a definitive confirmation once the current sample can be significantly enlarged, e.g. once the full *Gaia* results become available, with the expected significant increase in stars having reliable radial velocities, or the advent of future generation samples. Whether the results presented are a reflection of finely tuned hidden tertiary distributions, yet unknown astrometric systematics, or are indicative of a low acceleration modification in gravity is an interesting question which we can hope to answer over the next few years.

ACKNOWLEDGEMENTS

The authors thank an anonymous referee for constructive criticism leading to an enriched and clearer final version. The authors are indebted to Mike McCulloch for having originally suggested the collaboration, to Zac Plummer for his input in large data analysis and to Kareem El-Badry for his assistance implementing the ADQL query used. XH acknowledges financial assistance from DGAPA, UNAM grant IN106220 and CONACYT (*Consejo Nacional de Ciencia y Tecnología*). RAM. Cortés would like to acknowledge CONACYT for supporting this work through ascholarship. This work has used data from the European Space Agency (ESA) mission *Gaia* (<https://www.cosmos.esa.int/Gaia>), processed by the *Gaia* Data Processing and Analysis Consortium (DPAC, <https://www.cosmos.esa.int/web/Gaia/dpac/consortium>). Funding for the DPAC has been provided by national institutions, in particular the institutions participating in the *Gaia* Multilateral Agreement.

DATA AVAILABILITY

The data underlying this article will be shared on reasonable request to the corresponding author.

REFERENCES

- Banik I., Kroupa P., 2019, *MNRAS*, 487, 1653
 Banik I., Zhao H., 2018, *MNRAS*, 480, 2660
 Barrientos E., Mendoza S., 2018, *Phys. Rev. D*, 98, 084033
 Bekenstein J. D., 2004, *Phys. Rev. D*, 70, 083509
 Belokurov V. et al., 2020, *MNRAS*, in press
 Gaia Collaboration, 2020, *A&A*, 649, 20
 Capozziello S., de Laurentis M., 2011, *Phys. Rep.*, 509, 167
 Chae K.-H., Bernardi M., Domínguez Sánchez H., Sheth R. K., 2020a, *ApJ*, 903, L31
 Chae K.-H., Lelli F., Desmond H., McGaugh S. S., Li P., Schombert J. M., 2020b, *ApJ*, 904, 51
 Clarke C. J., 2020, *MNRAS*, 491, L72
 Durazo R., Hernandez X., Cervantes Sodi B., Sanchez S. F., 2018, *ApJ*, 863, 107
 El-Badry K., 2019, *MNRAS*, 482, 5018
 El-Badry K., Rix H.-W., 2018, *MNRAS*, 480, 4884
 Gaia Collaboration, 2016, *A&A*, 595, A1
 Gaia Collaboration, 2021, *A&A*, 649, A1
 Haghi H., Bazkiaei A. E., Zonoozi A. H., Kroupa P., 2016, *MNRAS*, 458, 4172
 Hernandez X., Lara D. I. A. J., 2020, *MNRAS*, 491, 272
 Hernandez X., Jiménez M. A., Allen C., 2012a, *Eur. Phys. J. C*, 72, 1884
 Hernandez X., Jiménez M. A., 2012b, *ApJ*, 750, 9
 Hernandez X., Cortés R. A. M., Allen C., Scarpa R., 2019a, *Int. J. Mod. Phys. D*, 28, 1950101
 Hernandez X., Sussman R. A., Nasser L., 2019b, *MNRAS*, 483, 147
 Jiang Y. F., Tremaine S., 2010, *MNRAS*, 401, 977
 Jiménez N. A., García G., Hernandez X., Nasser L., 2013, *ApJ*, 768, 142
 Kuijken K., Gilmore G., 1991, *ApJ*, 367, L9
 Lelli F., McGaugh S. S., Schombert J. M., Pawlowski M. S., 2017, *ApJ*, 836, 152
 Lindegren L. et al., 2021, *A&A*, 649, A2
 McCulloch M. E., Lucio J. H., 2019, *Astrophys. Space Sci.*, 364, 121
 McGaugh S. S., Schombert J. M., Bothun G. D., de Blok W. J. G., 2000, *ApJ*, 533, L99
 Milgrom M., 1983, *ApJ*, 270, 365
 Milgrom M., 2011, *AcPPB*, 42, 2175
 Moffat J. W., Toth V. T., 2008, *ApJ*, 680, 1158
 Penoyre Z., Belokurov V., Evans N. W., Everall A., Koposov S. E., 2020, *MNRAS*, 495, 321
 Pittordis C., Sutherland W., 2018, *MNRAS*, 480, 1778
 Pittordis C., Sutherland W., 2019, *MNRAS*, 488, 4740
 Scarpa R., Marconi G., Gilmozzi R., 2003, *A&A*, 405, L15
 Scarpa R., Ottolina R., Falomo R., Treves A., 2017, *Int. J. Mod. Phys. D*, 26, 1750067
 Shaya E. J., Olling R. P., 2011, *ApJS*, 192, 2
 Smart W. M., 1968, *Stellar Kinematics*. Wiley, New York
 Tian H.-J., El-Badry K., Rix H.-W., Gould A., 2020, *ApJS*, 246, 4
 Tokovinin A. A., Smekhov M. G., 2002, *A&A*, 382, 118
 Tokovinin A., Hartung M., Hayward T. L., 2010, *AJ*, 140, 510
 Verlinde E. P., 2016, *Sci. Post Phys.*, 2, 16
 Zhao H., Famaey B., 2010, *Phys. Rev. D*, 81, 087304

APPENDIX: NON-NEWTONIAN BINARIES

We here present a table giving the *Gaia* eDR3 identifiers and relevant data for the 128 wide binary pairs showing relative velocities above Newtonian expectations, those appearing in Fig. 8(a).

Table A1. Parameters for the binary stars appearing in Fig. 8(b).

<i>Gaia</i> eDR3 ID ₁	ϖ_1	$\sigma \varpi_1$	<i>Gaia</i> eDR3 ID ₂	ϖ_2	$\sigma \varpi_2$	ΔV_{RA}	$\sigma \Delta V_{\text{RA}}$	$\Delta V_{\text{Dec.}}$	$\sigma \Delta V_{\text{Dec.}}$	s
4725155516009856	9.668	0.0157	4724021644644224	9.686	0.0166	0.426	0.331	0.232	0.102	0.0148
36481628308083968	8.493	0.0197	36481593948346240	8.521	0.0149	0.059	0.163	0.405	0.090	0.0126
76300510625993344	16.631	0.0161	76300476266255488	16.637	0.0163	0.385	0.074	0.431	0.110	0.0101
98692614681349248	29.510	0.0224	98692339803443328	29.537	0.0179	0.337	0.027	0.258	0.011	0.0097
104998928046427264	16.623	0.0176	105004842216905344	16.653	0.0189	0.206	0.057	0.092	0.053	0.0324
153741691551129216	9.508	0.0165	153741760270606464	9.463	0.0164	0.361	0.052	0.102	0.048	0.0324
371552436752709504	17.577	0.0162	371552402392972032	17.557	0.0186	0.082	0.092	0.272	0.127	0.0098
507207363898475008	8.405	0.0112	507207329538738432	8.413	0.0136	0.353	0.065	0.059	0.030	0.0100
644549800855341184	10.808	0.0177	644549869574817792	10.814	0.0173	0.265	0.087	0.082	0.054	0.0114
680661782802091392	9.930	0.0192	680662573076074752	9.943	0.0195	0.183	0.030	0.159	0.043	0.0677
758958211973432704	14.957	0.0186	758958929232265472	14.981	0.0213	0.939	0.077	0.427	0.045	0.0280
796311542548505984	10.197	0.0180	796311954865365888	10.275	0.0164	0.811	0.259	0.246	0.047	0.0310
922601585552127104	15.912	0.0196	922595430863222144	15.878	0.0143	0.721	0.084	1.147	0.016	0.0495
992789150829982848	10.962	0.0161	992789872384490496	10.972	0.0181	0.219	0.069	0.494	0.067	0.0122
1021917447232306816	11.292	0.0132	1021917447232306944	11.315	0.0127	0.067	0.050	0.548	0.012	0.0094
1023887978228642176	10.788	0.0182	1023888012588380032	10.784	0.0191	0.295	0.175	0.465	0.094	0.0094
1055226293001395840	10.137	0.0126	1055226219986947200	10.101	0.0125	0.775	0.088	0.611	0.039	0.0267
1065304244783926400	9.242	0.0109	1065304068689257856	9.258	0.0109	0.001	0.117	0.136	0.043	0.0388
1112877875238798592	7.727	0.0189	1112877913895749888	7.693	0.0158	0.275	0.101	0.411	0.065	0.0190
1129061930485416960	10.839	0.0121	1129061797342364928	10.828	0.0117	0.089	0.115	0.901	0.026	0.0548
1142787168495168000	9.477	0.0108	1142786996696476288	9.485	0.0117	0.100	0.059	0.224	0.031	0.0183
1227417304334766208	8.263	0.0148	1227416514060783232	8.240	0.0142	0.180	0.092	0.422	0.040	0.0214
1346694146783637504	11.163	0.0092	1346694112423491712	11.156	0.0116	0.764	0.017	0.287	0.039	0.0111
1348285896022947584	20.547	0.0162	1348286651937191040	20.554	0.0108	0.152	0.031	0.021	0.010	0.0321
1509241238549271808	8.495	0.0127	1509241238549292800	8.479	0.0151	0.153	0.039	0.051	0.033	0.0246
1549521125478552064	20.469	0.0128	1549520949383005568	20.464	0.0153	0.076	0.013	0.045	0.027	0.0172
1580278623234613248	7.988	0.0097	1580278623234613376	7.979	0.0101	0.062	0.046	0.053	0.051	0.0094
1584402341594679808	13.138	0.0133	1584402479033634048	13.084	0.0153	0.426	0.028	0.236	0.041	0.0281
1585800851666242688	8.891	0.0115	1585800782946765312	8.895	0.0112	0.220	0.037	0.362	0.075	0.0228
1586977844504488576	29.624	0.0135	1586977737129182848	29.610	0.0115	0.252	0.009	0.188	0.018	0.0103
1661173816859019264	10.701	0.0110	1661174023017450112	10.716	0.0110	0.675	0.125	0.273	0.023	0.0394
1696726250465683968	8.822	0.0130	1696726319185160960	8.777	0.0124	0.897	0.066	0.262	0.053	0.0193
1700110684694632832	12.843	0.0113	1700112157867455232	12.863	0.0105	0.151	0.057	0.197	0.035	0.0095
1709320297168157824	9.003	0.0109	1709320292871977856	9.001	0.0105	0.524	0.029	0.009	0.057	0.0124
1719835231806217472	10.033	0.0116	1719835407900844544	10.042	0.0104	0.102	0.098	0.278	0.033	0.0411
1760471948915107200	13.272	0.0162	1760477618271932672	13.242	0.0189	0.049	0.024	0.024	0.050	0.0207
1778929480673414784	11.025	0.0195	1778930240883745536	11.069	0.0146	0.298	0.156	0.888	0.036	0.0302
1952145206786538112	9.554	0.0124	1952145172426798208	9.532	0.0136	0.179	0.110	0.032	0.087	0.0125
2140767560397457536	13.707	0.0109	2140767319879292160	13.717	0.0101	0.301	0.038	0.076	0.032	0.0352
2201834466266276864	10.213	0.0101	2201834470572701952	10.214	0.0101	0.024	0.030	0.036	0.062	0.0182
2211667368695978240	15.087	0.0117	2211667368695552896	15.068	0.0103	0.232	0.019	0.018	0.030	0.0106
2233231540491361408	15.150	0.0111	2233231330034854656	15.173	0.0102	0.455	0.010	0.116	0.022	0.0129
2260460155678348160	11.351	0.0107	2260460224397823488	11.337	0.0126	0.476	0.020	0.152	0.047	0.0127
2337837908524395776	8.443	0.0196	2337837908524639744	8.460	0.0195	0.010	0.123	0.521	0.034	0.0152
2386641518829641984	13.841	0.0196	2386641312671208960	13.837	0.0168	0.460	0.017	1.023	0.045	0.0552
2436430016675388160	7.951	0.0166	2436430119754603008	8.028	0.0175	1.006	0.192	0.625	0.094	0.0517
2514529598906714880	13.704	0.0230	2514541414361083648	13.776	0.0165	0.375	0.064	0.371	0.076	0.0237
2522327232292290688	18.212	0.0156	2522325548665111424	18.233	0.0195	0.271	0.021	0.233	0.036	0.0169
2592845200813026688	8.210	0.0128	2592845200813028992	8.183	0.0141	0.194	0.218	0.087	0.193	0.0187
2614582163441455616	8.876	0.0195	2614582064657951104	8.877	0.0190	0.234	0.200	0.338	0.179	0.0201
2663015998537909760	20.132	0.0172	2663015994242895488	20.130	0.0154	0.401	0.030	0.607	0.037	0.0118
2840600492363295616	14.914	0.0143	2840599633369837312	14.951	0.0137	0.104	0.032	0.063	0.035	0.0425
2989732545838913536	7.967	0.0156	2989735565198378368	7.958	0.0144	0.182	0.071	0.029	0.036	0.0563

Table A1 – *continued*

<i>Gaia</i> eDR3 ID ₁	ϖ_1	$\sigma \varpi_1$	<i>Gaia</i> eDR3 ID ₂	ϖ_2	$\sigma \varpi_2$	ΔV_{RA}	$\sigma \Delta V_{\text{RA}}$	$\Delta V_{\text{Dec.}}$	$\sigma \Delta V_{\text{Dec.}}$	s
3046204180298475264	11.459	0.0147	3046204150242468480	11.472	0.0156	0.045	0.092	0.143	0.046	0.0297
3072944474884690688	10.809	0.0160	3072920942760216064	10.825	0.0154	0.076	0.024	0.078	0.022	0.0468
3076534861386561536	14.437	0.0163	3076535243639085440	14.433	0.0169	0.541	0.112	0.484	0.072	0.0133
3158926322836178816	12.818	0.0138	3158878734598549376	12.814	0.0133	0.043	0.031	0.201	0.026	0.0532
3194720889516362880	8.318	0.0165	3194720786437148032	8.315	0.0146	0.295	0.153	0.206	0.048	0.0126
3199303963218457088	9.007	0.0158	3199303963218456832	8.948	0.0156	0.213	0.035	0.268	0.047	0.0227
3286839549942183168	8.441	0.0153	3286839932195653888	8.452	0.0155	0.115	0.125	0.389	0.020	0.0279
3371529368651025664	17.554	0.0185	3371529467432172672	17.581	0.0184	0.237	0.053	0.110	0.020	0.0154
3402090259984528768	13.321	0.0192	3402090466142958464	13.300	0.0243	0.298	0.047	0.279	0.036	0.0162
3431938839582893568	7.988	0.0197	3431938766565511424	8.053	0.0135	0.525	0.036	0.408	0.086	0.0305
3451267120128948992	24.064	0.0196	3451266742171824640	24.044	0.0225	0.487	0.015	0.205	0.010	0.0121
3497346209336507520	8.002	0.0260	3497346205040949248	8.085	0.0189	0.825	0.312	1.775	0.348	0.0160
3538247870092026624	13.531	0.0155	3538249588079338112	13.600	0.0233	0.038	0.092	0.006	0.024	0.0515
3550081879381593728	29.831	0.0262	3550084490721711872	29.799	0.0178	0.045	0.036	0.215	0.014	0.0382
3557719293306114560	17.682	0.0156	3557719293306114944	17.717	0.0160	0.113	0.077	0.141	0.034	0.0092
3731743568479226880	8.399	0.0181	3731742812564982912	8.393	0.0162	0.375	0.253	0.038	0.224	0.0136
3792739899447945216	9.297	0.0145	3792740006822516608	9.240	0.0150	0.206	0.078	0.762	0.163	0.0128
3836090722352641536	8.882	0.0221	3836090726648115968	8.856	0.0189	0.082	0.117	0.023	0.221	0.0147
3907643060734192896	17.653	0.0190	3907643060733826432	17.696	0.0191	0.040	0.166	0.292	0.020	0.0115
3975129194660883328	25.376	0.0270	3975223065466473216	25.375	0.0240	0.005	0.181	0.197	0.014	0.0140
4218533748765026560	12.139	0.0149	4218533959216594176	12.141	0.0142	0.300	0.105	0.408	0.099	0.0116
4395523033138822656	9.178	0.0197	4395522998779760128	9.204	0.0190	0.072	0.028	0.414	0.086	0.0102
4401991146507698944	7.787	0.0139	4401990394889506304	7.818	0.0117	0.317	0.061	0.288	0.035	0.0144
4404823011724525184	8.574	0.0191	4404823011724524416	8.586	0.0167	0.010	0.041	0.296	0.106	0.0125
4407544268641139712	9.432	0.0169	4407541313703639424	9.457	0.0170	0.517	0.045	0.213	0.059	0.0107
4430185068482324864	9.967	0.0140	4430185034123000960	9.986	0.0152	0.240	0.066	0.221	0.016	0.0214
4474801257476653952	8.125	0.0131	4474801218817508864	8.160	0.0121	0.055	0.023	0.104	0.043	0.0112
4545496243069399808	14.315	0.0146	4545496075567671808	14.311	0.0152	0.031	0.059	0.805	0.047	0.0148
4577272270853565952	10.531	0.0107	4577271961615916032	10.525	0.0130	0.175	0.063	0.395	0.033	0.0203
4584470739116877056	8.129	0.0133	4584470704757140096	8.151	0.0112	0.266	0.049	0.005	0.065	0.0435
4628920897552913792	9.532	0.0106	4628920970569782400	9.495	0.0099	0.330	0.085	0.085	0.045	0.0396
4629399567364049280	8.620	0.0108	4629399567364049664	8.597	0.0105	0.263	0.240	0.439	0.211	0.0124
4701607897573989248	10.438	0.0135	4701607893278187648	10.446	0.0112	0.589	0.078	0.127	0.060	0.0156
4729517591496033920	9.250	0.0096	4729517591496033152	9.226	0.0110	0.154	0.019	0.200	0.023	0.0098
4810651860180442624	10.972	0.0091	4810651928899919616	11.014	0.0098	0.170	0.010	0.186	0.088	0.0091
4813061852229522432	13.247	0.0101	4813061676134636928	13.273	0.0099	0.390	0.026	0.023	0.063	0.0154
4819741759028427904	8.253	0.0122	4819741763325357056	8.275	0.0136	1.958	0.027	0.334	0.023	0.0093
4822945740208994176	9.424	0.0118	4822945705849256192	9.423	0.0126	0.292	0.052	0.151	0.034	0.0118
4876470412926321280	9.184	0.0145	4876443990287014912	9.211	0.0115	0.146	0.073	0.025	0.053	0.0234
4879098280075566208	13.442	0.0108	4879098383154780672	13.461	0.0119	0.182	0.038	0.326	0.126	0.0154
4899504459972848512	13.027	0.0153	4899498069061515008	13.019	0.0155	0.117	0.036	0.002	0.169	0.0928
4902812787380558208	7.760	0.0145	4902812787380558976	7.781	0.0117	0.486	0.024	0.248	0.213	0.0096
4915145322115519104	8.021	0.0102	4915145322115519232	7.980	0.0103	0.008	0.021	0.371	0.019	0.0096
4981101348174544512	8.474	0.0116	4981101348174544768	8.433	0.0127	0.754	0.047	0.346	0.107	0.0201
5036326759219158272	9.258	0.0140	5035575758417810688	9.248	0.0142	0.025	0.033	0.120	0.061	0.0438
5099953023216735872	9.557	0.0157	5099953057577400704	9.553	0.0146	0.076	0.236	0.273	0.071	0.0314
5114547700047886976	11.807	0.0155	5114544745110388352	11.793	0.0145	0.058	0.175	0.098	0.087	0.0178
5179618511869510272	8.477	0.0155	5179618752387678592	8.463	0.0170	1.756	0.063	0.359	0.203	0.0659
5181911238426924288	8.353	0.0153	5181911234131665920	8.409	0.0162	0.342	0.051	0.226	0.035	0.0121
5269452631947873152	8.166	0.0091	5269452636245616128	8.130	0.0102	0.269	0.055	0.118	0.155	0.0169
5796674577807917184	20.093	0.0124	5796675471162119040	20.090	0.0139	0.158	0.007	0.141	0.016	0.0282
5800969407655752192	8.263	0.0115	5800969235854202496	8.289	0.0107	0.053	0.031	0.071	0.017	0.0402
5891531404470141824	38.998	0.0228	5891544873500692608	39.050	0.0145	0.151	0.050	0.035	0.043	0.0602

Table A1 – continued

<i>Gaia</i> eDR3 ID ₁	ϖ_1	$\sigma \varpi_1$	<i>Gaia</i> eDR3 ID ₂	ϖ_2	$\sigma \varpi_2$	ΔV_{RA}	$\sigma \Delta V_{\text{RA}}$	$\Delta V_{\text{Dec.}}$	$\sigma \Delta V_{\text{Dec.}}$	s
6078554071716755456	8.231	0.0171	6078554140436217728	8.269	0.0171	0.339	0.195	0.020	0.015	0.0871
6193279279612173952	33.480	0.0312	6193280031230266752	33.433	0.0227	0.053	0.085	0.292	0.020	0.0463
6206044369095120512	8.295	0.0190	6206045125009768192	8.356	0.0273	0.007	0.172	0.520	0.153	0.0157
6238116298643720192	7.778	0.0174	6238116298643719552	7.789	0.0155	0.182	0.057	0.128	0.062	0.0215
6249410860041044480	9.608	0.0202	6249411203638655232	9.647	0.0216	0.050	0.136	0.299	0.165	0.0442
6378374125048999424	9.181	0.0138	6378374052033393024	9.211	0.0124	0.555	0.075	0.029	0.031	0.0140
6398232816875801856	8.014	0.0142	6398232778219135744	8.022	0.0104	0.575	0.150	0.151	0.124	0.0240
6447718261829058816	10.914	0.0164	6447718467987494784	10.918	0.0171	0.056	0.173	0.248	0.054	0.0351
6458626310529028352	13.330	0.0129	6458626271874014208	13.315	0.0130	0.027	0.060	0.009	0.013	0.0292
6464392012066637440	9.391	0.0146	6464391977706899712	9.385	0.0163	0.168	0.024	0.153	0.020	0.0390
6562582828536563328	10.555	0.0142	6562581969543104640	10.554	0.0120	0.020	0.179	0.046	0.053	0.0623
6586315275923449856	8.471	0.0211	6586315207203972224	8.504	0.0215	0.136	0.190	0.285	0.085	0.0182
6615293145390228352	8.513	0.0189	6615291667921479552	8.535	0.0178	1.031	0.055	0.867	0.028	0.0125
6620898657532005120	29.995	0.0148	6620893645304242176	29.959	0.0200	0.059	0.067	0.222	0.044	0.0262
6639645128923820160	10.611	0.0135	6639645128923818624	10.626	0.0145	0.007	0.011	0.028	0.012	0.0114
6658696396962053120	8.362	0.0180	6658696401257998464	8.365	0.0159	0.223	0.045	0.256	0.018	0.0179
6681883211702702208	8.539	0.0194	6681883039904009856	8.595	0.0174	0.329	0.120	0.550	0.042	0.0203
6695911949280082432	9.200	0.0151	6695911880560604672	9.193	0.0134	0.424	0.082	0.151	0.032	0.0102
6768864992462040832	14.645	0.0135	6768865714016553344	14.623	0.0144	0.385	0.051	0.037	0.036	0.0261
6812424241536340864	21.290	0.0367	6812422832786523776	21.189	0.0178	2.871	0.134	0.590	0.013	0.0281
6840365718216434816	14.041	0.0222	6840365615137220096	14.038	0.0158	0.319	0.070	0.083	0.066	0.0219
6859531958238411904	12.022	0.0180	6859531752079979776	11.999	0.0233	0.011	0.025	0.287	0.061	0.0458

Note. The first three columns give *Gaia* eDR3 identifiers, parallax, and parallax errors for the primaries, while the following three columns give the corresponding information for the secondaries. Columns 7–10 give relative velocities for the pair in RA, the error in this quantity, relative velocities for the pair in Dec., and the error for this quantity. The final column shows the projected separation on the pane of the sky for each binary pair. Units for parallaxes, velocities and separations are mas, km s^{−1}, and pc, respectively.

This paper has been typeset from a \LaTeX file prepared by the author.